Industrial Chemistry & Materials

ROYAL SOCIETY OF CHEMISTRY

PAPER

View Article Online
View Journal | View Issue

Cite this: *Ind. Chem. Mater.*, 2025, **3**, 567

Fine-tuned ultramicroporous carbon materials *via* CO_2 activation for molecular sieving of fluorinated propylene and propane†

Yiwen Fu,‡[ab] Liangzheng Sheng,‡[a] Wei Xia,[a] Guangtong Hai,*[ab] Jialei Yan,[a] Lihang Chen,*[ab] Qiwei Yang,[ab] Zhiguo Zhang,[ab] Qilong Ren[ab] and Zongbi Bao*[ab]

Ultramicroporous carbon materials with precisely engineered pore structures offer a promising pathway for the challenging separation of fluorinated gases with similar physicochemical properties, such as C_3F_6 (fluorinated propylene) and C_3F_8 (fluorinated propane). In this work, we report the synthesis of CO_2-activated porous carbon adsorbents derived from a precursory resin and systematically investigate their molecular sieving behavior for C_3F_6/C_3F_8 mixtures. Through controlled thermal pyrolysis and stepwise CO_2 activation, we tailored ultramicropore size distributions to selectively exclude or admit target molecules. Adsorption studies reveal that optimal CO_2 activation yields pore sizes that enable effective separation of C_3F_6 from C_3F_8, achieving efficient molecular sieving due to size exclusion effects. Excessive activation, however, generates larger pores that diminish selectivity due to nonspecific affinity for both gases. The findings highlight the importance of ultramicropore control for energy-efficient separation of fluorinated hydrocarbons and provide insights for designing advanced adsorbents for industrial gas purification.

Keywords: Electronic specialty gas (ESGs); Adsorption separation; Phenolic resin-derived carbon; Molecular sieving; C_3F_6/C_3F_8.

Received 10th May 2025,
Accepted 23rd June 2025

DOI: 10.1039/d5im00079c

rsc.li/icm

1 Introduction

The semiconductor industry, serving as the foundational infrastructure for artificial intelligence (AI) and 5G ecosystems, has achieved atomic-scale fabrication breakthroughs that critically depend on ultrapure electronic specialty gases (ESGs). These gases enable advanced manufacturing processes,[1] with their purity demonstrating a direct correlation to process yield metrics as semiconductor nodes evolve.[2] Perfluoropropane (C_3F_8), a plasma etching and chemical vapor deposition (CVD) chamber-cleaning agent, is widely employed due to its etch selectivity and nanoscale aspect ratio control.[3,4] However, industrial production of C_3F_8, typically achieved through the fluorination of hexafluoropropylene (C_3F_6), invariably results in the presence of 1–10 mol% impurities.[5,6] The minimal boiling point differential (ΔT_{bp} = 5.7 K) between C_3F_6 and C_3F_8 renders conventional distillation economically unsustainable for achieving semiconductor-grade purity (5 N/6 N), necessitating energy-intensive multi-column configurations.[7,8]

Adsorptive molecular sieving has emerged as an innovative alternative to fluorocarbon distillation, circumventing thermodynamic limitations through pore-size precision engineering.[9,10] This approach necessitates precise control of pore sizes within the 5.0–8.0 Å range, positioned between the three-dimensional dimensions of C_3F_6 (7.3 Å × 6.2 Å × 5.1 Å) and C_3F_8 (7.6 Å × 5.3 Å × 5.1 Å).[11] However, commercial zeolite adsorbents exhibit limited tunability in pore aperture dimensions at the angstrom scale. Moreover, their inherent cation polarization fields promote strong π-complexation with C_3F_6,[7,12,13] resulting in energy-intensive, high-temperature regeneration requirements and an increased risk of undesirable olefin polymerization.[14–16] In contrast, although a select group of metal–organic frameworks (MOFs) including Al-PMA,[17] Zn-bzc-CF_3 (ref. 18) and CoFA[19] have demonstrated sieving separation for C_3F_6/C_3F_8 *via* programmable pore environments, their practical application is constrained by metastable coordination bonds, elevated synthesis costs, and irreversible framework collapse during processing.[20–22] By comparison, carbon molecular

[a] *Key Laboratory of Biomass Chemical Engineering of Ministry of Education, College of Chemical and Biological Engineering, Zhejiang University, 38 Zheda Road, Hangzhou 310027, P. R. China. E-mail: fyw7814@163.com, 12360004@zju.edu.cn, 12028027@zju.edu.cn, haigt@zju.edu.cn, 12428005@zju.edu.cn, chenlihang@zju.edu.cn, yangqw@zju.edu.cn, zhiguo.zhang@zju.edu.cn, renql@zju.edu.cn, baozb@zju.edu.cn*

[b] *Zhejiang Key Laboratory of F-contained Functional Materials, Institute of Zhejiang University-Quzhou, 99 Zheda Road, Quzhou 324000, P. R. China*

† Electronic supplementary information (ESI) available. See DOI: https://doi.org/10.1039/d5im00079c

‡ These authors contributed equally to this work.

sieves (CMS) leverage defect-engineered architectures to facilitate physisorption dominated by van der Waals interactions, thereby enabling simplified desorption.[23–25] Their well-developed porosity and tailorable pore architectures position them as industrial benchmarks for the high-efficiency separation of C_3F_6 and C_3F_8 through molecular sieving mechanisms.

Traditional carbon-based adsorbents, such as those derived from coal, suffer from significant structural heterogeneity attributed to variable feedstock compositions, stochastic pyrolysis, and uncontrolled etching during activation, leading to broad pore size distributions.[26–28] Such intrinsic limitations preclude effective molecular sieving for near-isomorphic fluorocarbons like C_3F_6/C_3F_8. Conversely, synthetic resin-derived carbons offer improved structural predictability due to their periodic crosslinked networks.[29–31] Notably, phenolic resin-derived carbons have demonstrated the potential to engineer microporosity for industrial-scale air (N_2/O_2) and CO_2/N_2 separation,[32–34] inspiring efforts to develop targeted narrow-pore architectures for C_3F_6/C_3F_8 separation.

Nevertheless, the inherent pore size distribution in resin-derived carbons restricts the separation of larger fluorocarbon molecules. Additionally, ultra-micropores with narrowly confined dimensions often result in sluggish adsorption kinetics and protracted equilibration times.[35–37] To address this, recent strategies have focused on directionally modulating pore structures to optimize the balance between molecular sieving and diffusivity. For instance, the incorporation of hierarchical mesopores has been explored to expand pore networks and enhance gas diffusion in carbon matrices.[38] Xiao *et al.* demonstrated that hydrothermal temperature modulation enables the synthesis of GC-x materials with tailored micropore expansion, promoting accelerated C_3H_6 diffusion kinetics while preserving effective C_3H_8 exclusion.[39] Such defect-engineered, pore-expansion strategies quantitatively resolve the trade-off between selectivity and diffusion efficiency, offering a universal framework for industrial gas separations with carbon molecular sieves.

Common chemical activation methods are often associated with significant environmental and operational challenges, such as toxic emissions, hazardous waste production, and severe equipment corrosion.[40] Instead, physical activation provides a more environmentally benign alternative.[41] For example, Li's group employed a synergistic CO_2-steam activation strategy for pore size regulation, wherein CO_2 primarily governs micropore expansion and optimizes pore architectures.[42] Inspired by these insights, we report herein a series of phenolic resin-derived carbon molecular sieves (PRC) synthesized *via* CO_2 physical activation, enabling precise modulation of surface characteristics and pore architecture. By carefully tuning the CO_2 concentration (5–25 vol%) during pyrolysis, we produce carbon materials exhibiting monodisperse ultra-micropores (5.6–8.0 Å) and graded porosity. The resulting appropriate pore size facilitated precision size-sieving of C_3F_8 concomitant with accelerated kinetic diffusion of C_3F_6 (Scheme 1). The optimized PRC-15CO_2 achieves an exceptional C_3F_6 adsorption capacity (2.34 mmol g^{-1} at 100 kPa), outstanding dynamic breakthrough performance, and complete C_3F_8 exclusion under ambient conditions—marking the first carbon material to achieve efficient C_3F_6/C_3F_8 sieving separation, surpassing even state-of-the-art MOFs. Additionally, these slightly expanded micropore channels enhance mass transfer kinetics, while ultra-high selectivity is corroborated by molecular dynamics (MD) simulations. The industrial viability of these materials is further substantiated by their cyclic stability, batch-to-batch reproducibility, scalable synthesis, and cost-effectiveness. The successful integration of precision pore engineering with sustainable activation methodologies thus establishes carbon molecular sieves as a disruptive technology for the purification of semiconductor-grade fluorocarbons, addressing critical challenges in next-generation electronics manufacturing.

2 Results and discussion

Phenolic resin (PR) was synthesized *via* an emulsion polymerization method by following the previously reports with some modification.[43] Subsequent carbonization under controlled CO_2/N_2 atmospheres (0–25 vol% CO_2) yielded

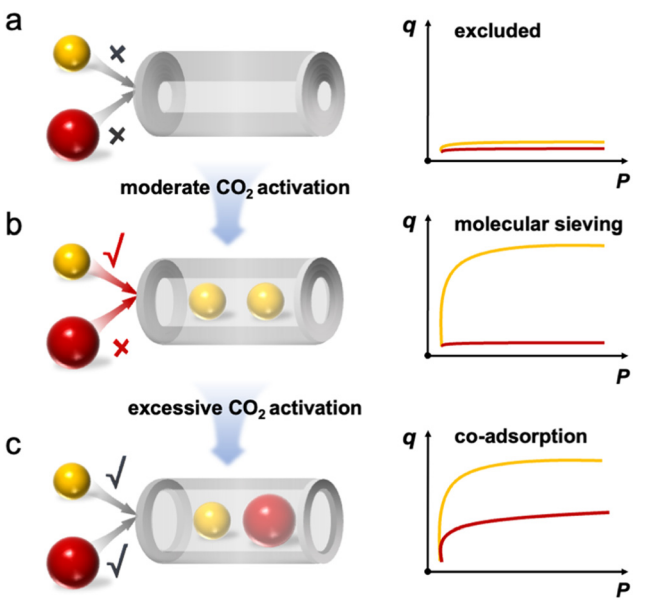

Scheme 1 Schematic illustration of the synthesis of CO_2-activated phenolic resin-derived carbon adsorbents and the proposed mechanism of controlled thermal pyrolysis for the development of ultramicropores tailored for C_3F_6 (yellow spheres)/C_3F_8 (red spheres) molecular sieving separation: (a) narrow pores exclude both C_3F_6 and C_3F_8; (b) appropriately sized pores, obtained through moderate CO_2 activation, enable the selective molecular sieving of C_3F_6/C_3F_8; (c) excessively large pores, resulting from extensive CO_2 activation, display strong affinity toward both C_3F_6 and C_3F_8, thereby reducing selectivity.

spherical carbon particles with uniform particle size distributions (2–5 μm), as evidenced by scanning electron microscopy (SEM) (Fig. 1a and b). The progressive evolution of surface roughness, attributed to CO_2-mediated etching, clearly demonstrates the active role of CO_2 in modulating both the chemical composition and the topology of the carbon structures. This is further substantiated by energy-dispersive X-ray spectroscopy (EDS) depth profiling, revealing a volcano-shaped dependence of the C/O ratio on CO_2 concentration (Fig. 1c and d and Table S1†). Furthermore, X-ray photoelectron spectroscopy (XPS) elucidated a coordinated surface reconstruction process, wherein native C–O (286.9 eV) and C–N (285.0 eV) groups are converted to C═O (288.6 eV) and O–C═O (290.0 eV) species. The observed inconsistency between nitrogen content (higher in elemental analysis, Table S1†) and oxygen functional group abundance (higher in XPS, Table S2†) originated from intrinsic bulk-surface differences in carbon materials. Specifically, nitrogen atoms distribute uniformly throughout the bulk matrix, whereas oxygen-containing functional groups preferentially accumulate at surfaces. This discrepancy is further amplified by XPS's collective detection of multiple oxygen functionalities (C–O, C═O, and O–C═O). The total content of C═O and O–C═O peaks at 5 vol% CO_2 (Fig. 1e and S1 and Table S2†), mirroring Fourier-transform infrared spectroscopy (FTIR) observations of quinoid group formation (Fig. 1f) and high-resolution O 1s XPS spectra (Fig. S2 and Table S3†). Newly formed quinone-type C═O groups (1670 cm^{-1}) emerged, with oxygen functionalities displaying a marked volcano-shaped trend (maxima at 5 vol% CO_2), highlighting the dual function of CO_2 as both etchant and oxidizer. Moreover, the apparent contradiction between the reduced FTIR features (Fig. 1f) and higher oxygen content (Table S1†) in highly activated samples (PRC-15CO_2 and PRC-25CO_2) is attributed to graphitization-induced peak broadening, the low IR-activity of stable oxygen groups, and conductivity-related background interference.[44–46] In parallel, the carbon matrix exhibited increased ordering, as evidenced by an elevated sp^2/sp^3 hybridization ratio and the appearance of graphitic nitrogen species (Fig. S3 and Table S4†), collectively enhancing π-electron delocalization across the carbon lattice.

The observed non-monotonic behavior in structural evolution originates from a dual mechanism paradigm governed by the CO_2 partial pressure. At CO_2 concentrations below 5 vol%, selective oxidation prevails, effectively removing metastable oxygen functionalities (C–O–C and C═O) while preserving graphitic domains. This is reflected in Raman spectral analysis by a decrease in the I_D/I_G ratio from 0.971 to 0.943 (Fig. 1g), indicative of enhanced

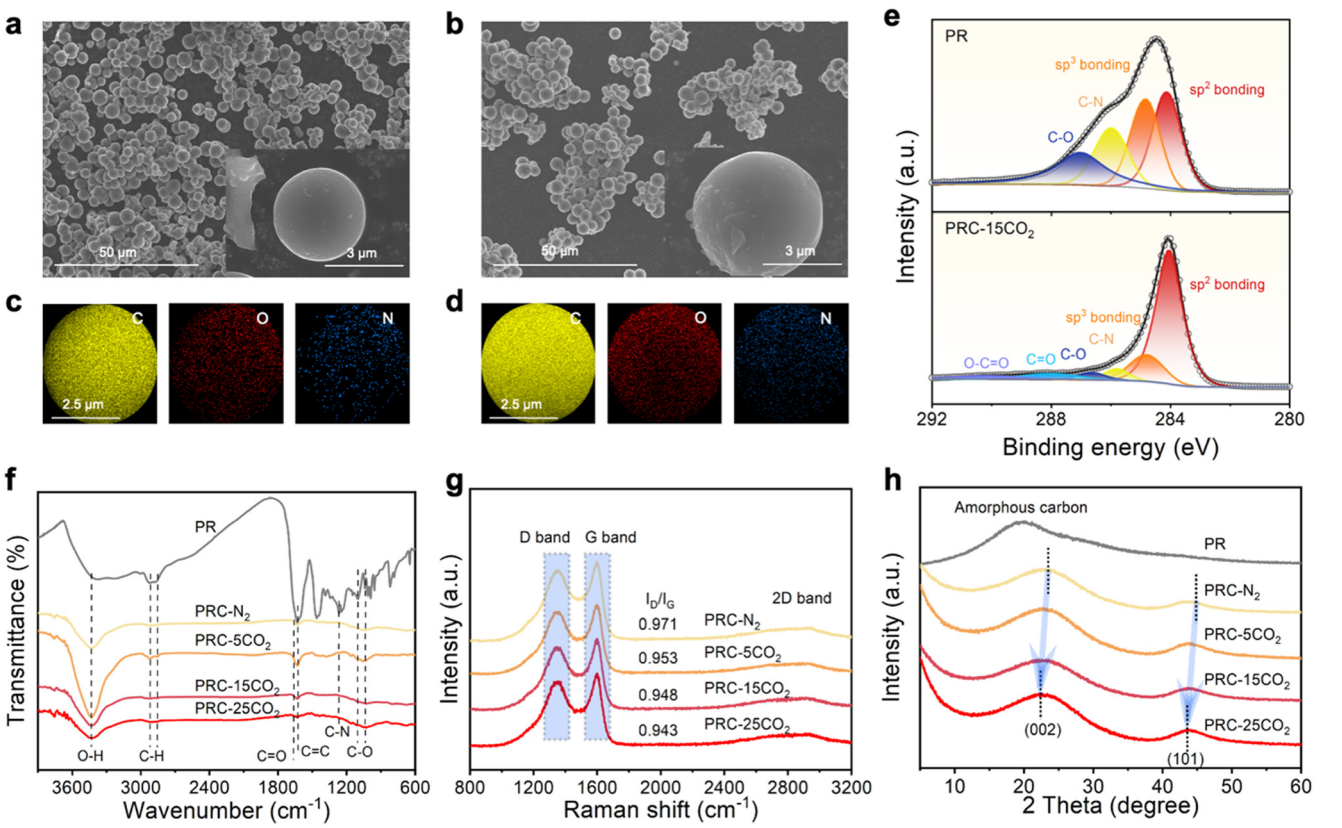

Fig. 1 SEM images of (a) PRC-N_2 and (b) PRC-15CO_2; elemental mapping images of C, O and N of (c) PRC-N_2 and (d) PRC-15CO_2; (e) high-resolution spectra of C 1s for phenolic resin and PRC-15CO_2; (f) FTIR spectra, (g) Raman spectra and (h) X-ray diffraction patterns of phenolic resin precursor and its derived carbon molecular sieves (PRC-N_2, PRC-5CO_2, PRC-15CO_2, and PRC-25CO_2).

structural order. In contrast, above 5 vol% CO_2, the Boudouard equilibrium becomes thermodynamically favorable, leading to framework gasification and the generation of microstructural defects. This transition is evidenced by significant increases in specific surface area (ΔS_{BET} = +202.43 $m^2\ g^{-1}$) and pore volume expansion (ΔV_{pore} = +0.090 $cm^3\ g^{-1}$) (Fig. S4 and Table S5†), demonstrating the concentration-dependent shift in CO_2's role from selective etchant to bulk oxidizer. Complementary powder X-ray diffraction (PXRD) analysis (Fig. 1h) further delineates crystallographic evolution: the inclusion of CO_2 induces a continuous shift of the (002) and (101) Bragg reflections toward lower angles, corresponding to lattice expansion. This structural reorganization, driven by preferential etching of amorphous carbon regions, aligns with Raman data indicating improved graphitic ordering.

The diverse physicochemical transformations prompted by varying CO_2 treatments motivated detailed investigation of pore structural evolution using N_2 adsorption–desorption measurements at 77 K (Fig. 2a). All PRC materials exhibited type I isotherms with fully reversible adsorption–desorption profiles (no hysteresis), confirming dominant microporosity. The resulting specific surface area and pore volume clearly reflect the role of CO_2 activation in pore expansion. Narrow pore size distribution (PSD) profiles (Fig. 2a) reveal the prevalence of ultra-micropores (5–7 Å), strategically matched to the kinetic diameters of C_3F_6 and C_3F_8. Notably, CO_2-activated carbon molecular sieves maintain PSD profiles akin to N_2-annealed variants (PRC-N_2), although with distinct evolutionary trends: PRC-5CO_2 exhibits initial micropore expansion with the appearance of a broader shoulder (7–9 Å), which becomes more prominent in PRC-15CO_2 ($V_{>7Å}$ = 0.039 $cm^3\ g^{-1}$) (Table S5†) due to Boudouard reaction-driven oxidation. This CO_2 concentration-dependent pore architecture integrates ultra-micropores (5–7 Å) for molecular sieving and progressively expanded micropores (7–9 Å) for enhance diffusion, correlating strongly with improved C_3F_6/C_3F_8 separation efficiency.

Adsorption isotherms for C3 fluorocarbons (Fig. 2b and c) quantitatively assess the influence of CO_2 partial pressure on gas uptake. PRC-25CO_2 exhibits the highest C_3F_6 saturation capacity (2.77 mmol g^{-1} at 100 kPa), but with significant co-adsorption of C_3F_8 (1.17 mmol g^{-1}). This underscores a thermodynamic trade-off: excessive framework etching compromises selectivity by permitting target product loss, emphasizing the necessity for precise pore engineering. In contrast, PRC-5CO_2 and PRC-15CO_2, achieve nearly exclusive C_3F_8 exclusion (0.02–0.03 mmol g^{-1}), while maintaining substantial C_3F_6 uptake (1.16 and 2.34 mmol g^{-1}, respectively). The almost negligible adsorption observed with PRC-N_2 confirms that CO_2-mediated pore expansion is essential for generating channels (>5.6 Å) accessible to fluorocarbons. Under saturation, PRC-15CO_2 attains an

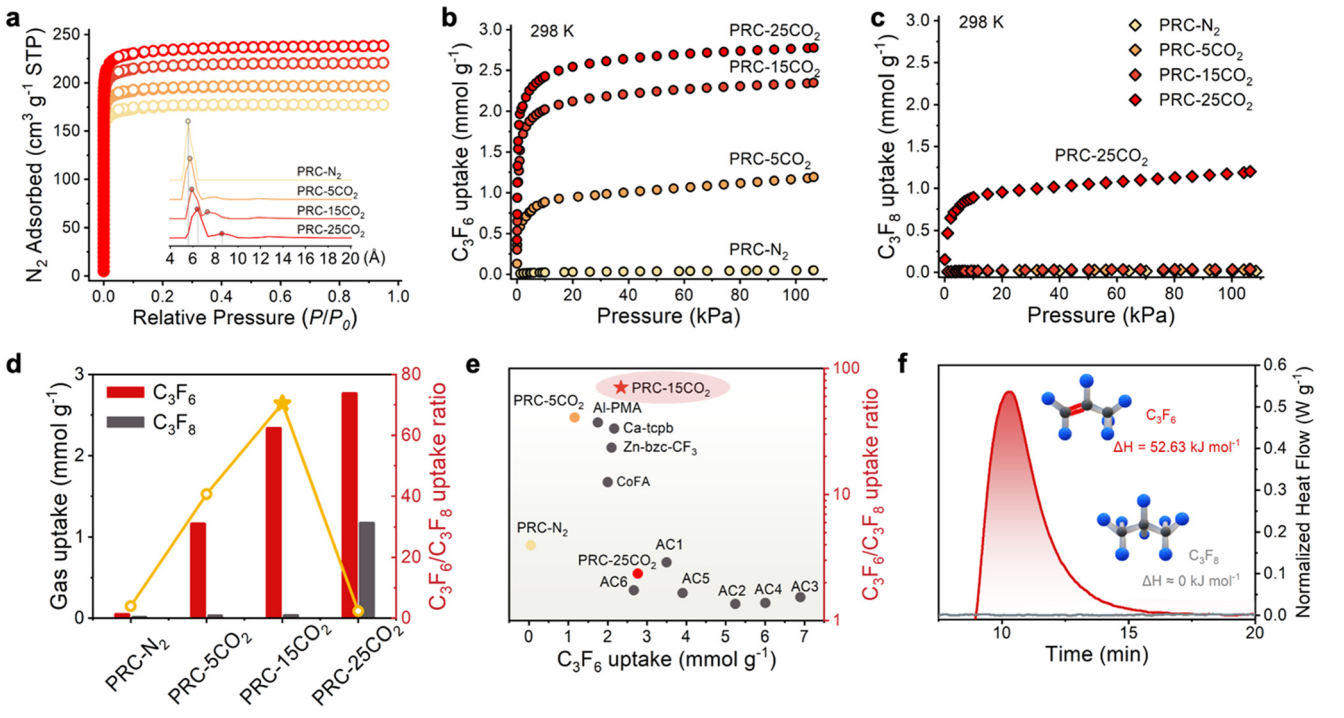

Fig. 2 (a) N_2 adsorption–desorption isotherms at 77 K (the curves from top to bottom correspond to PRC-25CO_2, PRC-15CO_2, PRC-5CO_2 and PRC-N_2) and pore size distributions of phenolic resin-derived carbon molecular sieve materials; adsorption isotherms of (b) C_3F_6 and (c) C_3F_8 at 298 K on PRC materials; (d) adsorption isobars (100 kPa) for C_3F_6 (red) and C_3F_8 (grey), along with the uptake ratio of C_3F_6/C_3F_8 (yellow) for PRC materials; (e) adsorbent properties for C_3F_6/C_3F_8 separation at 298 K and 100 kPa; (f) adsorption heats for C_3F_6 and C_3F_8 on PRC-15CO_2 as determined by TG-DSC.

exceptional uptake ratio of 70.48, well exceeding that of PRC-5CO_2 (40.72) and PRC-25CO_2 (2.36) (Fig. 2d). This hierarchy affirms that optimal CO_2 activation (15 vol%) achieves a fine balance between pore expansion and molecular sieving, averting the capacity-selectivity trade-off manifest in over-etched materials.

A comparative assessment against commercial carbon adsorbents (Fig. 2e and S5 and Table S6†) revealed systemic limitations of these materials, characterized by pervasive co-adsorption behavior that significantly undermines both selectivity and process economics. For instance, activated carbon AC3 exhibited the highest C_3F_6 adsorption capacity (6.90 mmol g^{-1}) but demonstrated marginal selectivity (1.53). Among the evaluated carbons, AC1 achieved the highest uptake ratio (2.90), which remains orders of magnitude inferior to that of PRC-15CO_2. Moreover, PRC-15CO_2 surpassed all reported MOFs in uptake ratio, outperforming CoFA (12.5), Zn-bzc-CF_3 (23.5) and Ca-tcpb (33.3) under identical conditions (298 K and 100 kPa). This dual parameter superiority in both capacity and selectivity establishes PRC-15CO_2 as a disruptive alternative to coordination polymers for fluorocarbon purification.

The observed disparities in adsorption behavior can be rationalized by differences in affinity between adsorbents and adsorbates, as evaluated through thermogravimetry-differential scanning calorimetry (TG-DSC). The heat of adsorption (Q_{st}) for C_3F_6 on PRC-15CO_2 was precisely determined to be 52.63 kJ mol^{-1}, while C_3F_8 exhibited undetectable interaction, attributable to size exclusion imposed by the micropores of PRC-15CO_2 (Fig. 2f). This moderate Q_{st} surpasses those of other commercial carbons (Fig. S6 and S7†), positioning PRC-15CO_2 as a readily regenerable adsorbent suitable for industrial separation processes.

To further validate kinetic sieving capabilities, time-dependent uptake profiles for C_3F_6 and C_3F_8 were recorded (Fig. 3a and b). Adsorption equilibrium times for C_3F_6 decreased markedly with increasing CO_2 concentration, from 1200 min for PRC-5CO_2 to 34 min for PRC-25CO_2. Correspondingly, the diffusion time constant (D') followed the order PRC-5CO_2 (7.49×10^{-5} s^{-1}) < PRC-15CO_2 (9.15×10^{-4} s^{-1}) < PRC-25CO_2 (3.42×10^{-3} s^{-1}) (Fig. S8 and Table S7†). Given the non-polar nature of the carbon pore interface, differences in diffusion rates primarily arise from variations in pore size. Pore expansion enhances mass transfer efficiency and reduces diffusion energy barrier by synergistically increasing porosity, average pore size, and the proportion of effective micropores (<7 Å). Meanwhile, the higher density of delocalized π electrons creates stronger van der Waals and π–π interaction sites for C_3F_6, imposing surface diffusion limitations. Although PRC-25CO_2 exhibits excessive pore expansion, it still maintains a C_3F_6/C_3F_8 kinetic selectivity of 8.51, indicating preserved albeit reduced separation capability. However, the co-adsorption of C_3F_8 on PRC-25CO_2 remains significant, whereas PRC-15CO_2 achieves complete C_3F_8 exclusion. These results demonstrate that

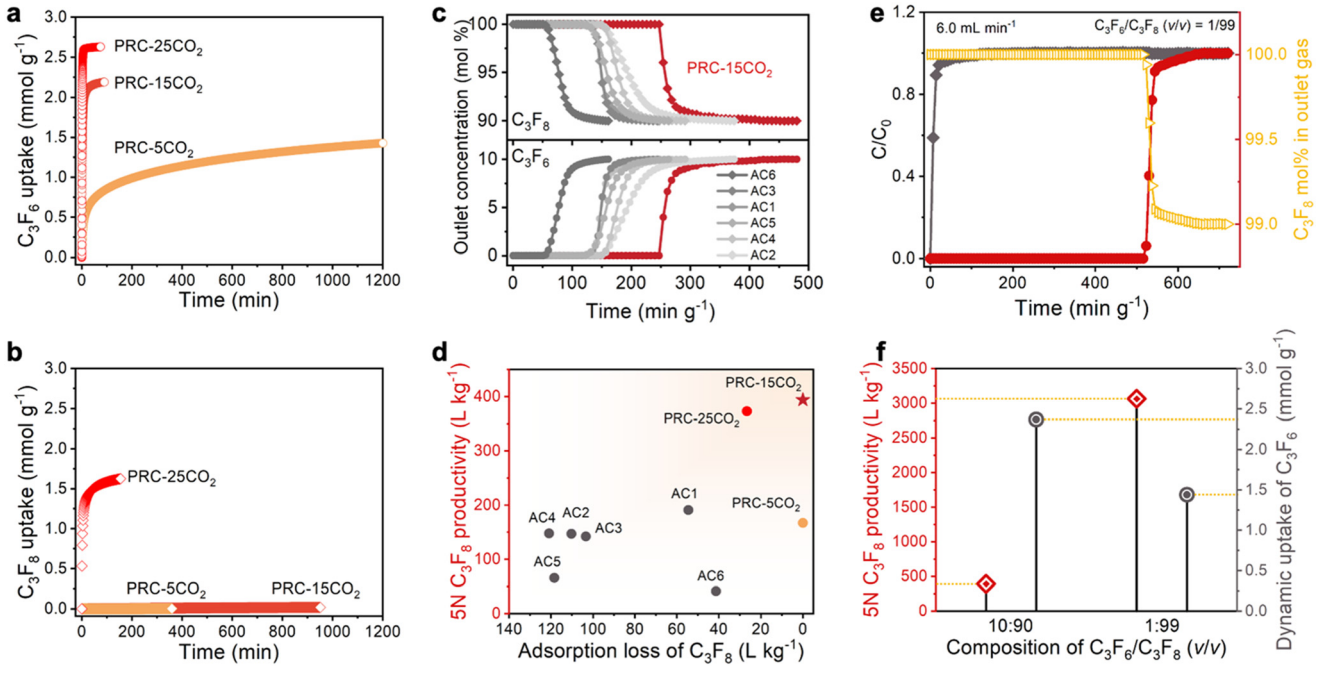

Fig. 3 Time-dependent uptake profile of (a) C_3F_6 and (b) C_3F_8 on PRC-5CO_2, PRC-15CO_2 and PRC-25CO_2 at 298 K and 100 kPa; (c) comparison of the dynamic breakthrough performance of these carbon-based adsorbents for C_3F_6/C_3F_8 mixtures (10/90, v/v) at 298 K and 100 kPa; (d) comparative analysis of C_3F_8 adsorption loss and the yield of high purity C_3F_8 (>5 N) from a single breakthrough experiment using the aforementioned adsorbents; (e) experimental breakthrough curves for C_3F_6/C_3F_8 (1/99, v/v) on PRC-15CO_2 at 298 K and 100 kPa; (f) comparison of the dynamic adsorption capacity for C_3F_6 and the yield of 5 N C_3F_8 obtained by PRC-15CO_2 following breakthrough with different feed gases.

precision micropore engineering fundamentally dictates optimal separation performance.

To assess industrial applicability, dynamic breakthrough experiments were conducted under conditions representative of crude distillation mixtures (C_3F_6/C_3F_8, 10/90, v/v). In PRC-15CO_2 columns, C_3F_8 eluted immediately, whereas C_3F_6 was retained for 218.82 min g^{-1} (Fig. 3c). During this period, effluent C_3F_6 concentration remained below 0.001%, enabling the production of ultra-high purity C_3F_8 (>5 N, 99.999%) with a yield of 393.88 L kg^{-1}. This performance surpasses that of other commercial carbon materials (*e.g.*, AC1: 190.91 L kg^{-1}, AC2: 147.01 L kg^{-1}) and other PRC materials (Fig. 3d and S9–S11; Tables S8 and S9†). Under more dilute impurity conditions (C_3F_6/C_3F_8, 1/99, v/v), RC-15CO_2 maintained sharp separation, yielding 3063.73 L kg^{-1} of 5 N-grade C_3F_8 (Fig. 3e and f). Moreover, implementation of multi-column units operating in series facilitates continuous production of high-purity C_3F_8.

Mechanistically, a multilayer carbon model with controlled interlayer spacings (5.6, 6.5, 8.0 Å), mimicking the pore size distribution, was constructed to elucidate the molecular sieving mechanism. Molecular dynamics (MD) simulations conducted at 298 K and 0.1 MPa tracked diffusion of a binary C_3F_6/C_3F_8 (10/90, v/v) mixture through these engineered architectures. Time-resolved adsorption snapshots (Fig. 4a–c and S12–S14†) reveal progressive differentiation in molecular transport. Within the initial 1000 ps, C_3F_6 molecules adsorbed preferentially *via* quadrupole moment interactions, while C_3F_8 showed no adsorption. Between 1000 and 10 000 ps, C_3F_6 rotated and diffused through 6.5 Å interlayer channels (PRC-15CO_2), with complete exclusion of C_3F_8 (kinetic diameter ϕ = 7.6 Å > slit width) (Fig. 4e). By 10 000 ps, full C_3F_6 permeation and absolute C_3F_8 exclusion was achieved, theoretically ensuring 5 N-grade C_3F_8 purity. Simulations across different interlayer spacings further highlighted critical pore size thresholds: 5.6 Å slits (PRC-5CO_2) caused molecular bottlenecks due to diffusion barriers, precluding passage of both species (Fig. 4d), whereas 8.0 Å slits (PRC-25CO_2) allowed unselective passage, confirming the importance of controlled CO_2-mediated activation (Fig. 4f). The presence of strategically incorporated oxygen functionalities coupled with optimized pore sizes in PRC-15CO_2 supports a dual-function mechanism facilitating both molecular sieving precision and adsorption enhancement, as corroborated experimentally and by MD simulations.

Material stability and regenerability are critical for industrial deployment. After five consecutive static/dynamic adsorption–desorption cycles (180 °C degassing for 4 h), PRC-15CO_2 retained 99.5% of initial C_3F_6 adsorption capacity while consistently producing 5 N-grade C_3F_8 (3063.73 ± 15.21 L kg^{-1}), exhibiting negligible degradation (Fig. S15† and 5c). Thermogravimetric analysis under N_2 atmosphere revealed high thermal stability with minimal mass loss, contrasting markedly with the phenolic resin precursor (Fig. S16†), and maintained exceptional stability in air. Thus, CO_2-modulated carbonization effectively suppresses deleterious side reactions, preserving graphitic domain integrity. Furthermore, the engineered hydrophobicity increased progressively with CO_2 concentration, reflecting enhanced graphitization and a reduction in hydrophilic oxygen species (C–O). Achieving a water contact angle of 129.6°, governed by the Cassie–

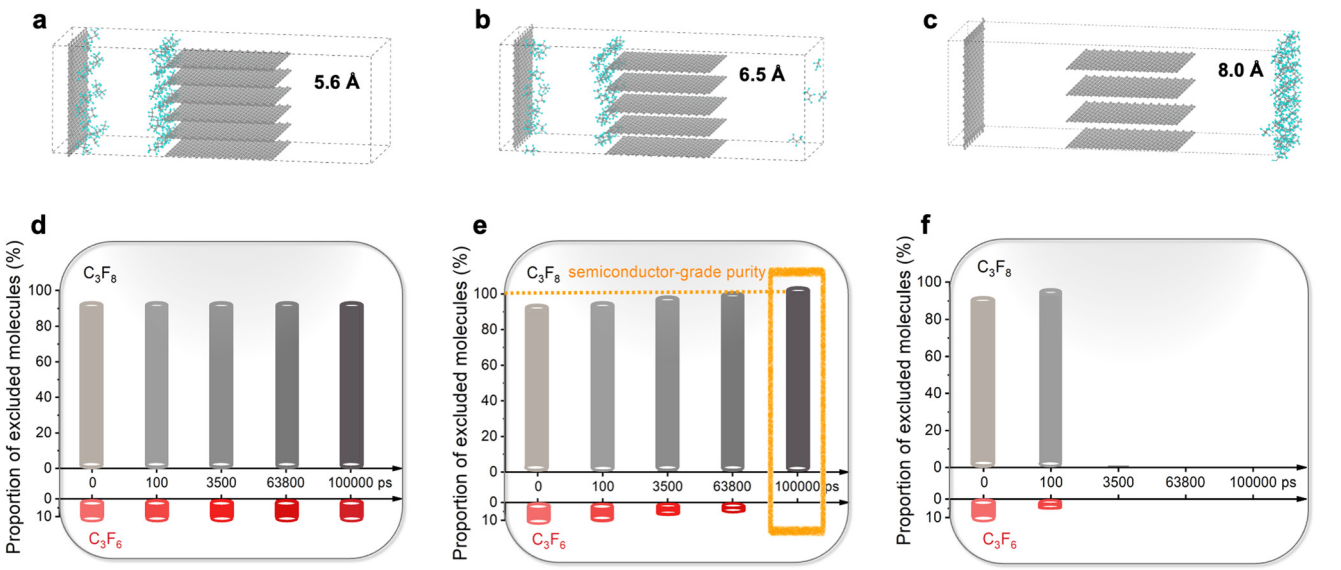

Fig. 4 MD simulation snapshots of the adsorption process for a C_3F_6/C_3F_8 (10/90, v/v) mixture in (a) PRC-5CO_2, (b) PRC-15CO_2 and (c) PRC-25CO_2 models at the final simulation time; (d–f) proportion of excluded gas molecules in the inlet stream over time for (d) PRC-5CO_2, (e) PRC-15CO_2, and (f) PRC-25CO_2, respectively (the *Y*-axis represents the proportion of C_3F_6 or C_3F_8 molecule in the total number of molecules at the entrance).

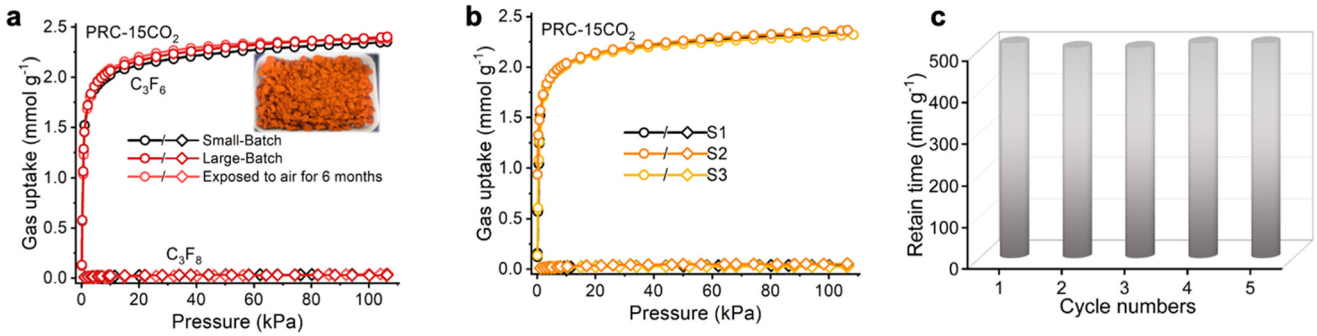

Fig. 5 (a) Comparison of the adsorption isotherms for C_3F_6 and C_3F_8 at 298 K on PRC-15CO_2 synthesized under varying conditions; (b) adsorption isotherms of C_3F_6 and C_3F_8 at 298 K on phenolic resin-derived carbon molecular sieve materials synthesized across different batches; (c) multicycle dynamic breakthrough curves of C_3F_6/C_3F_8 (1/99, v/v) gas mixtures using a packed column bed with PRC-15CO_2 at 298 K and 100 kPa, illustrating the retention times over five dynamic cycles.

Baxter model, this super-hydrophobicity and elevated H_2O adsorption barriers confer significant moisture resistance (Fig. S17†).

Scaling synthesis was demonstrated through seamless transition from laboratory to pilot-scale synthesis (10-fold precursor scale-up), yielding kilogram-scale batches that retained performance and met industrial stability benchmarks, including extended shelf life (Δq < 1.5% loss after 6 months) (Fig. 5a and S18†). Furthermore, batch-to-batch reproducibility across three production lots exhibited minimal variation in C_3F_6 and C_3F_8 uptake, attributable to precision pyrolysis protocols and defect engineering *via* controlled CO_2 etching optimizing microporosity (Fig. 5b and S19†). This holistic integration of surface chemistry control, statistical process management, and scalable manufacturing establishes PRC-15CO_2 as a paradigm-shifting material that overcomes longstanding challenges in carbon molecular sieve industrialization by synchronizing atomic-scale functionality with macroscopic production robustness.

3 Conclusions

In summary, we demonstrate that careful regulation of ultramicropore dimensions in CO_2-activated carbon adsorbents is essential for achieving effective molecular sieving of fluorinated propylene (C_3F_6) from fluorinated propane (C_3F_8). The results show that moderate CO_2 activation produces tailored pore structures that selectively favor C_3F_6 over C_3F_8, whereas excessive activation generates larger pores with reduced selectivity. This work not only underscores the pivotal role of ultramicroporous engineering in boosting separation performance, but also provides a rational strategy for the development of advanced adsorbents for challenging small-molecule separations in industrial settings. The CO_2 activation method offers a scalable route for the preparation of molecular sieves tailored to specific separation needs, advancing the sustainable purification of valuable fluorinated gases.

4 Experimental section

4.1 Materials

All reagents, solvents and gases were purchased from commercial sources and used as received without further purification. Resorcinol ($C_6H_6O_2$, 99.5%), anhydrous sodium carbonate (Na_2CO_3, 99.5%), polyethylene glycol (PEG-2000, CP), hexamethylenetetramine (HMTA, $C_6H_{12}N_4$, 98.0%) and formaldehyde solution (AR, containing polymerization inhibitor) were supplied by Sinopharm Chemical Reagent Co., Ltd. Activated carbons AC1 (general adsorption use), AC2 (electroplating decolorization grade), AC3 (BPL), AC4 (100CTC3070), AC5 and AC6 (coconut and fruit shells origins) were provided by Calgon Carbon Corporation. High-purity gases including N_2, He, CO_2, C_3F_6, C_3F_8 (all 99.999%), as well as premixed gas blends of CO_2/N_2 (5/95, 15/85, 25/75, v/v) and C_3F_6/C_3F_8 (10/90, 1/99, v/v) were supplied by Zhejiang Quzhou City Julun Gas Co., Ltd.

4.2 Preparation of materials

4.2.1 Synthesis of phenolic resin (PR). Phenolic resin (PR) was synthesized *via* a modified emulsion polymerization method. Specifically, resorcinol (10.00 ± 0.05 g) was dissolved in 200 mL deionized water within a 500 mL three-neck flask under vigorous stirring (500 rpm) at 353 K. After complete dissolution, Na_2CO_3 (0.05 g), PEG-2000 (1.00 g) and HMTA (12.00 g) were sequentially added. The mixture was homogenized, then 20 mL of formaldehyde aqueous solution was introduced dropwise. The reaction was maintained under reflux for 24 h with precise temperature control (±1 °C). The resulting PR was isolated by hot filtration, followed by washing with deionized water and ethanol to remove residual monomers and surfactants. The purified product was vacuum-dried at 348 K for 12 h, yielding orange-yellow PR powder with moisture content below 0.5%.

4.2.2 Scale-up synthesis of PR. Scaling the above protocol tenfold, resorcinol (100.0 g) was dissolved in 3 L deionized water in a 5 L reactor under identical agitation and thermal conditions. Na_2CO_3 (0.50 g), PEG-2000 (10.00 g) and HMTA

(120.00 g) were added, followed by the controlled dropwise addition of 200 mL formaldehyde solution over 30 min. The reaction time was extended to 72 h under reflux to accommodate scale kinetics. Post-reaction purification entailed gravitational sedimentation (six cycles, 2 h per cycle) with water replacement to remove colloidal impurities, ethanol washing (5 × 200 mL) and vacuum drying at 348 K for 12 h, yielding PR powder with consistent physicochemical properties.

4.2.3 Synthesis of phenolic resin-derived carbon (PRC). Precisely 2.00 g of PR powder was loaded into a quartz boat located at the isothermal zone of a horizontal tubular furnace. Carbonization was conducted with a heating rate of 5 °C min^{-1} from ambient temperature to 900 °C under varied atmospheres: PRC-N_2 (pure N_2, 99.999%), PRC-5CO_2 (CO_2/N_2, 5/95, v/v), PRC-15CO_2 (CO_2/N_2, 15/85, v/v), and PRC-25CO_2 (CO_2/N_2, 25/75, v/v) at a total gas flow rate of 75 mL min^{-1}, followed by natural cooling to below 50 °C.

4.3 Characterization of PRC

Surface topography and elemental composition were analyzed using a field-emission scanning electron microscope (Hitachi Regulus 8230) equipped with EDS attachment. Powder X-ray diffraction (PXRD) was performed on a PANalytical X'Pert PRO diffractometer with Cu Kα radiation (λ = 1.542 Å), scanning 5–60° with a step size of 0.02°. Raman spectroscopy was performed on a Horiba LabRAM Odyssey spectrometer with a 532 nm laser source covering 500–4000 cm^{-1}. XPS was carried out using a Kratos AXIS Supra+ spectrometer with monochromatic Al Kα X-rays (1486.6 eV). FT-IR spectra were recorded in attenuated total reflectance (ATR) mode on a Bruker INVENIO R system (4000–600 cm^{-1}, 2 cm^{-1} resolution, 32 scans). Thermogravimetric analysis (TGA) was investigated on a Pyris 1 TGA Thermogravimetric analyzer (TA Instruments Corp., USA) to 900 °C under N_2 or air at a heating rate of 10 °C min^{-1}. Nitrogen adsorption–desorption isotherms at 77 K were collected on a Micromeritics ASAP 3Flex analyzer after degassing at 200 °C under vacuum for 24 h, yielding BET surface areas and pore size distributions. Elemental analysis employed an Elementar Vario MAX cube analyzer.

4.4 Gas adsorption measurements

Single-component adsorption isotherms of C_3F_6 and C_3F_8 were measured using a Micromeritics ASAP 2020 PLUS gas sorption analyzer at 298.0 ± 0.1 K over pressures from 0 to 100 kPa. Approximately 0.100 ± 0.005 g of sample was degassed at 250 °C under vacuum for 6 h prior to analysis. Samples were transferred under protected atmosphere to prevent contamination. PRC adsorbents exhibited negligible C_3F_8 uptake (<0.05 mmol g^{-1} at 100 kPa), enabling use of equilibrium adsorption capacity ratios as primary selectivity indicators.

4.5 Measurements of adsorption heats (Q_{st})

Adsorption heats (Q_{st}) were quantified using coupled thermogravimetric-differential scanning calorimetry (TGA-DSC, STD 650). Approximately 10.0 ± 0.2 mg of sample was loaded into a platinum crucible and degassed *in situ* under N_2 (50 mL min^{-1}) with a linear heating ramp (10 K min^{-1}) to 473 K, followed by thermal equilibration. Thermal equilibration was maintained until mass fluctuation fell below 0.01% min^{-1}. The system was cooled to 313 K at 5 K min^{-1} under continuous N_2 flow and stabilized for 30 min before alternate introduction of C_3F_6 and C_3F_8 gases. Mass change and heat flow were monitored, equilibrium was defined as DSC signal variation <2 μW over 300 s.

4.6 Dynamic multicomponent breakthrough experiments

Degassed samples (200 °C, 24 h) were packed into stainless steel columns (50 mm × 4.6 mm I.D.) inside an argon-filled glovebox (H_2O < 0.1 ppm, O_2 < 0.5 ppm) to prevent contamination. Columns were thermally conditioned at 200 °C under helium purge for 6 h, then integrated into a temperature-controlled breakthrough apparatus maintained at 298 K. Gas mixtures of C_3F_6/C_3F_8 (10/90, v/v) and (1/99, v/v) were introduced at flow rates of 2.0 and 6.0 mL min^{-1}, respectively. Effluent composition was monitored by a Shimadzu GC-2010 Pro gas chromatography. Regeneration involved thermal desorption at 200 °C under N_2 flow for 12 h.

4.7 Adsorption kinetic experiments

Kinetic uptake curves were recorded using an Intelligent Gravimetric Analyzer (IGA-001) with a high-resolution microbalance. Samples (50.0–80.0 mg) were pre-activated *in situ* under dynamic vacuum at 200 °C ± 0.5 °C until mass stabilization, then equilibrated at 298.0 ± 0.1 K *via* closed-loop thermostatic control. Following adsorbate introduction, gravimetric data acquisition continued until saturation. Transport diffusivities and kinetic selectivities were derived from time-dependent uptake profiles.

4.8 Molecular dynamics (MD) simulations

Molecular dynamics (MD) simulations employed the GROMACS platform,[47] parameterized with the generalized Amber force field (GAFF). Atomic partial charges were assigned *via* the restrained electrostatic potential (RESP) method, and long-range van der Waals and electrostatic interactions were treated using the particle mesh Ewald (PME) algorithm.[48,49] Systems were energy-minimized to a convergence of 0.01 kcal mol^{-1}, then equilibrated at 298 K in the NVT ensemble using a Nosé–Hoover thermostat.[50,51] Production rans spanned 100 ns with 1 fs timestep, incorporating a 10.3 MPa transmembrane pressure gradient to model gas permeation dynamics while maintaining molecular stochasticity.

4.9 Vapor adsorption measurements

Moisture adsorption characteristics were evaluated on a Belsorp-max II vapor sorption analyzer. Prior to analysis, samples underwent standardized degassing protocols. Measurements were conducted isothermally at 303 K.

4.10 Stability tests

Adsorption stability was assessed through five consecutive C_3F_6 adsorption–desorption cycles and five consecutive dynamic breakthrough adsorption–regeneration cycles under controlled experimental conditions.

Data availability

The data supporting this article have been included as part of the ESI.†

Author contributions

Yiwen Fu: data curation, investigation, writing – original draft and review. Liangzheng Sheng: methodology, data curation, validation and writing – original draft. Guangtong Hai: methodology, data curation and validation. Jialei Yan: validation, investigation and data curation. Lihang Chen: validation, investigation, review, editing, supervision and funding acquisition. Zhiguo Zhang: resources, project administration and funding acquisition. Qiwei Yang: resources, project administration and funding acquisition. Qilong Ren: resources, project administration and funding acquisition. Zongbi Bao: conceptualization, editing, supervision, resources, project administration and funding acquisition.

Conflicts of interest

The authors declare no conflict of interest.

Acknowledgements

The authors acknowledge the support of the National Natural Science Foundation of China (No. 22225802, 22208288, 22421004, 22141001, 22288102, U24A20532), the Zhejiang Provincial Natural Science Foundation of China (No. LZ22B060002, LQ22B060005) and Zhejiang Provincial Innovation Center of Advanced Chemicals Technology (2024SJCZX0020).

References

1 J. R. Clark, Chemistry of electronic gases, *J. Chem. Educ.*, 2006, **83**, 857.
2 S. S. Kaler, Q. Lou, V. M. Donnelly and D. J. Economou, Silicon nitride and silicon etching by CH_3F/O_2 and CH_3F/CO_2 plasma beams, *J. Vac. Sci. Technol., A*, 2016, **34**, 41301.
3 W. S. Yang, W. K. Kim, D. H. Yoon, J. W. Lim, M. Isshiki and H. Y. Lee, Surface roughness of Ti: $LiNbO_3$ etched by Ar/C_3F_8 plasma and annealing effect, *J. Vac. Sci. Technol., B: Microelectron. Nanometer Struct.–Process., Meas., Phenom.*, 2006, **24**, 675–677.
4 L. Z. Sheng, W. Xia, Y. W. Fu, J. L. Yan, Z. Z. Zhou, F. Zheng, F. X. Shen, L. H. Chen, Z. G. Zhang, Q. W. Yang, Q. L. Ren and Z. B. Bao, Temperature-responsive molecular sieving of fluorinated propylene and propane via a flexible metal-organic framework with high-density open metal sites, *ACS Mater. Lett.*, 2025, **7**, 2080–2087.
5 A. J. Sicard and R. T. Baker, Fluorocarbon refrigerants and their syntheses: Past to present, *Chem. Rev.*, 2020, **120**, 9164–9303.
6 R. T. Tsaix, H. P. Chen and W. Y. Hsien, A review of uses, environmental hazards and recovery/recycle technologies of perfluorocarbons (PFCs) emissions from the semiconductor manufacturing processes, *J. Loss Prev. Process Ind.*, 2002, **15**, 65–75.
7 H. S. Lee, N. S. Kim, D. Kwon, S. K. Lee, S. K. Numanx, T. Jung, T. Chox, M. Mazur, H. S. Cho and C. Jo, Post-synthesis functionalization enables fine-tuning the molecular-sieving properties of zeolites for light olefin/paraffin separations, *Adv. Mater.*, 2021, **33**, 2105398.
8 J. B. Lin, T. T. T. Nguyen, R. Vaidhyanathan, J. Burner, J. M. Taylor, H. Durekova, F. Akhtar, R. K. Mah, O. Ghaffari-Nik, S. Marx, N. Fylstra, S. S. Iremonger, K. W. Dawson, P. Sarkar, P. Hovington, A. Rajendran, T. K. Woo and G. K. H. Shimizu, A scalable metal-organic framework as a durable physisorbent for carbon dioxide capture, *Science*, 2021, **374**, 1464–1469.
9 F. Q. Chen, X. L. Huang, K. Q. Guo, L. Yang, H. R. Sun, W. Xia, Z. G. Zhang, Q. W. Yang, Y. W. Yang, D. Zhao, Q. L. Ren and Z. B. Bao, Molecular sieving of propylene from propane in metal–organic framework-derived ultramicroporous carbon adsorbents, *ACS Appl. Mater. Interfaces*, 2022, **14**, 30443–30453.
10 S. J. Luo, T. L. Han, C. Wang, Y. Sun, H. J. Zhang, R. L. Guo and S. J. Zhang, Hierarchically microporous membranes for highly energy-efficient gas separations, *Ind. Chem. Mater.*, 2023, **3**, 376–387.
11 W. Xia, Z. Z. Zhou, L. Z. Sheng, L. H. Chen, F. Zheng, Z. J. Zhang, Z. G. Zhang, Q. W. Yang, Q. L. Ren and Z. B. Bao, Deep purification of perfluorinated electronic specialty gas with a scalable metal–organic framework featuring tailored positive potential traps, *Sci. Bull.*, 2025, **70**, 232–240.
12 C. Han, J. Yang, S. Dong, L. Ma, Q. Dai and J. Guo, Zeolite preparation from industrial solid waste: Current status, applications, and prospects, *Sep. Purif. Technol.*, 2025, **354**, 128957.
13 J. D. Monzón, A. M. Pereyra, M. R. Gonzalez, M. S. Legnoverde, M. S. Moreno, N. Gargiulo, A. Peluso, P. Aprea, D. Caputo and E. I. Basaldella, Ethylene adsorption onto thermally treated AgA-zeolite, *Appl. Surf. Sci.*, 2021, **542**, 148748.
14 M. C. Campo, A. M. Ribeiro, A. Ferreira, J. C. Santos, C. Lutz, J. M. Loureiro and A. E. Rodrigues, New 13X zeolite for propylene/propane separation by vacuum swing adsorption, *Sep. Purif. Technol.*, 2013, **103**, 60–70.

15 P. Ji, J. B. Solomon, Z. Lin, A. M. Wilders, R. F. Jordan and W. Lin, Transformation of metal–organic framework secondary building units into hexanuclear Zr-alkyl catalysts for ethylene polymerization, *J. Am. Chem. Soc.*, 2017, **139**, 11325–11328.

16 V. Blay, B. Louis, R. Miravalles, T. Yokoi, K. A. Peccatiello, M. Clough and B. Yilmaz, Engineering zeolites for catalytic cracking to light olefins, *ACS Catal.*, 2017, **7**, 6542–6566.

17 W. Xia, Y. S. Yang, L. Z. Sheng, Z. Z. Zhou, L. H. Chen, Z. J. Zhang, Z. G. Zhang, Q. W. Yang, Q. L. Ren and Z. B. Bao, Temperature-dependent molecular sieving of fluorinated propane/propylene mixtures by a flexible-robust metal-organic framework, *Sci. Adv.*, 2024, **10**, eadj6473.

18 M. Z. Zheng, W. J. Xue, T. G. Yan, Z. F. Jiang, Z. Fang, H. L. Huang and C. L. Zhong, Fluorinated MOF-based hexafluoropropylene nanotrap for highly efficient purification of octafluoropropane electronic specialty gas, *Angew. Chem., Int. Ed.*, 2024, **63**, e202401770.

19 W. Xia, Z. Z. Zhou, L. Z. Sheng, L. H. Chen, F. X. Shen, F. Zheng, Z. G. Zhang, Q. W. Yang, Q. L. Ren and Z. B. Bao, Bioinspired recognition in metal-organic frameworks enabling precise sieving separation of fluorinated propylene and propane mixtures, *Nat. Commun.*, 2024, **15**, 8716.

20 N. Lamia, M. Jorge, M. A. Granato, F. A. Almeida Paz, H. Chevreau and A. E. Rodrigues, Adsorption of propane, propylene and isobutane on a metal–organic framework: Molecular simulation and experiment, *Chem. Eng. Sci.*, 2009, **64**, 3246–3259.

21 N. C. Burtch, H. Jasuja and K. S. Walton, Water stability and adsorption in metal–organic frameworks, *Chem. Rev.*, 2014, **114**, 10575–10612.

22 H. Chu, Z. Liu, C. C. Wang and P. Wang, Sustainable production and applications of metal–organic frameworks, *Chem. Commun.*, 2024, **60**, 8350–8359.

23 M. Andrade, A. J. Parnell, G. Bernardo and A. Mendes, Propane selective carbon adsorbents from phenolic resin precursor, *Microporous Mesoporous Mater.*, 2021, **320**, 111071.

24 J. Castro-Gutiérrez, E. De Oliveira Jardim, R. L. S. Canevesi, J. Silvestre-Albero, M. Kriesten, M. Thommes, A. Celzard and V. Fierro, Molecular sieving of linear and branched C6 alkanes by tannin-derived carbons, *Carbon*, 2021, **174**, 413–422.

25 J. Wang, W. X. Fu, L. M. Wang, Y. L. Li, Y. P. Li, Z. Y. Sui and X. F. Xu, Modulation of pore structure in a microporous carbon for enhanced adsorption of perfluorinated electron specialty gases with efficient separation, *Chem. Eng. J.*, 2023, **477**, 147128.

26 J. Laine and S. Yunes, Effect of the preparation method on the pore size distribution of activated carbon from coconut shell, *Carbon*, 1992, **30**, 601–604.

27 D. P. Kumar, D. Ramesh, V. K. Vikraman and P. Subramanian, Synthesis of carbon molecular sieves from agricultural residues: Status, challenges and prospects, *Environ. Res.*, 2022, **214**, 114022.

28 I. Mochida, S. H. Yoon and J. Miyawaki, Current features of traditional carbon materials, *Carbon*, 2015, **93**, 1079.

29 F. Q. Chen, X. L. Huang, L. Yang, Z. G. Zhang, Q. W. Yang, Y. W. Yang, D. Zhao, Q. L. Ren and Z. B. Bao, Boosting xenon adsorption with record capacity in microporous carbon molecular sieves, *Sci. China: Chem.*, 2023, **66**, 601–610.

30 J. Liu, E. M. Calverley, M. H. McAdon, J. M. Goss, Y. Liu, K. C. Andrews, T. D. Wolford, D. E. Beyer, C. S. Han, D. A. Anaya, R. P. Golombeski, C. F. Broomall, S. Sprague, H. Clements and K. F. Mabe, New carbon molecular sieves for propylene/propane separation with high working capacity and separation factor, *Carbon*, 2017, **123**, 273–282.

31 F. Q. Chen, K. Q. Guo, X. L. Huang, Z. G. Zhang, Q. W. Yang, Y. W. Yang, Q. L. Ren and Z. B. Bao, Extraction of propane and ethane from natural gas on ultramicroporous carbon adsorbent with record selectivity, *Sci. China Mater.*, 2023, **66**, 319–326.

32 Z. L. Yu, Y. C. Gao, B. Qin, Z. Y. Ma and S. H. Yu, Revitalizing traditional phenolic resin toward a versatile platform for advanced materials, *Acc. Mater. Res.*, 2024, **5**, 146–159.

33 F. Jiao, Activation-free preparation of porous carbon fiber derived from phenolic resin for CO_2 absorption, *J. Taiwan Inst. Chem. Eng.*, 2024, **162**, 105621.

34 D. Torres, S. Pérez-Rodríguez, L. Cesari, C. Castel, E. Favre, V. Fierro and A. Celzard, Review on the preparation of carbon membranes derived from phenolic resins for gas separation: From petrochemical precursors to bioresources, *Carbon*, 2021, **183**, 12–33.

35 Q. Ding, Z. Zhang, P. Zhang, J. Wang, X. Cui, C. H. He, S. Deng and H. Xing, Control of intracrystalline diffusion in a bilayered metal-organic framework for efficient kinetic separation of propylene from propane, *Chem. Eng. J.*, 2022, **434**, 134784.

36 S. K. Verma and P. L. Walker, Alteration of molecular sieving properties of microporous carbons by heat treatment and carbon gasification, *Carbon*, 1990, **28**, 175–184.

37 X. Z. Chu, Z. P. Cheng, Y. J. Zhao, J. M. Xu, M. S. Li, L. Zhou and C. H. Lee, Adsorption dynamics of hydrogen and deuterium in a carbon molecular sieve bed at 77K, *Sep. Purif. Technol.*, 2015, **146**, 168–175.

38 Y. F. Yuan, Y. S. Wang, X. L. Zhang, W. C. Li, G. P. Hao, L. Han and A.-H. Lu, Wiggling mesopores kinetically amplify the adsorptive separation of propylene/propane, *Angew. Chem., Int. Ed.*, 2021, **60**, 19063–19067.

39 S. Du, J. Huang, A. W. Anjum, J. Xiao and Z. Li, A novel mechanism of controlling ultramicropore size in carbons at sub-angstrom level for molecular sieving of propylene/propane mixtures, *J. Mater. Chem. A*, 2021, **9**, 23873–23881.

40 M. Sevilla, N. Díez and A. B. Fuertes, More sustainable chemical activation strategies for the production of porous carbons, *ChemSusChem*, 2021, **14**, 94–117.

41 H. Teng and S. C. Wang, Preparation of porous carbons from phenol–formaldehyde resins with chemical and physical activation, *Carbon*, 2000, **38**, 817–824.

42 Y. Li, L. Lu, S. Lyu, H. Xu, X. Ren and Y. A. Levendis, Activated coke preparation by physical activation of coal and biomass co-carbonized chars, *J. Anal. Appl. Pyrolysis*, 2021, **156**, 105137.

43 J. Przepiórski, B. Tryba and A. W. Morawski, Adsorption of carbon dioxide on phenolic resin-based carbon spheres, *Appl. Surf. Sci.*, 2002, **196**, 296–300.
44 J. Y. Cheng, Z. L. Yi, Z. B. Wang, F. Li, N. N. Gong, A. Ahmad, X. Q. Guo, G. Song, S. T. Yuan and C. M. Chen, Towards optimized Li-ion storage performance: Insight on the oxygen species evolution of hard carbon by H_2 reduction, *Electrochim. Acta*, 2020, **337**, 135736.
45 M. Weisenberger, I. M. Gullon, J. V. Agullo, H. V. Rizo, C. Merino, R. Andrews, D. L. Qian and T. Rantell, The effect of graphitization temperature on the structure of helical-ribbon carbon nanofibers, *Carbon*, 2009, **47**, 2211–2218.
46 K. F. Mak, M. Y. Sfeir, Y. Wu, C. H. Lui, J. A. Misewich and T. F. Heinz, Measurement of the optical conductivity of graphene, *Phys. Rev. Lett.*, 2008, **101**, 196405.
47 J. Wang, R. M. Wolf, J. W. Caldwell, P. A. Kollman and D. A. Case, Development and testing of a general amber force field, *J. Comput. Chem.*, 2004, **25**, 1157–1174.
48 C. I. Bayly, P. Cieplak, W. Cornell and P. A. Kollman, A well-behaved electrostatic potential based method using charge restraints for deriving atomic charges: The RESP model, *J. Phys. Chem.*, 1993, **97**, 10269–10280.
49 U. Essmann, L. Perera, M. L. Berkowitz, T. Darden, H. Lee and L. G. Pedersen, A smooth particle mesh ewald method, *J. Chem. Phys.*, 1995, **103**, 8577–8593.
50 W. G. Hoover, Canonical dynamics: Equilibrium phase-space distributions, *Phys. Rev. A: At., Mol., Opt. Phys.*, 1985, **31**, 1695.
51 S. Nosé, A molecular dynamics method for simulations in the canonical ensemble, *Mol. Phys.*, 2002, **100**, 191–198.